Title: Estimating snow depth by combining satellite data and ground-based observations over Alaska: A deep learning approach

Authors: Jiwen Wang [a], Qiangqiang Yuan [a*], Huanfeng Shen [c,d,e], Tingting Liu [g*], Tongwen Li [c], Linwei Yue [b], Xiaogang Shi [h], Liangpei Zhang [d,f]

Affiliations:

[a] School of Geodesy and Geomatics, Wuhan University, Wuhan, Hubei, 430079, China.

[b] Faculty of Information Engineering, China University of Geosciences, Wuhan, Hubei, 430079, China.

[c] School of Resource and Environmental Sciences, Wuhan University, Wuhan, Hubei, 430079, China.

[d] The Collaborative Innovation Center for Geospatial Technology, Wuhan, Hubei, 430079, China.

[e] The Key Laboratory of Geographic Information System, Ministry of Education, Wuhan University, Wuhan, Hubei, 430079, China.

[f] The State Key Laboratory of Information Engineering in Surveying, Mapping and Remote Sensing, Wuhan University, Wuhan, Hubei, 430079, China.

[g] The Chinese Antarctic Center of Surveying and Mapping, Wuhan University, Wuhan, Hubei, 430079, China.

[h] University of Glasgow, Glasgow, Scotland, G128QQ, United Kingdom.

Email address:

wangjiwen@whu.edu.cn (Jiwen Wang), yqiang86@gmail.com (Qiangqiang Yuan), shenhf@whu.edu.cn (Huanfeng Shen), ttliu23@ whu.edu.cn (Tingting Liu), litw@whu.edu.cn (Tongwen Li), yuelw@cug.edu.cn (Linwei Yue), John.Shi@glasgow.ac.uk (Xiaogang Shi), zlp62@whu.edu.cn (Liangpei Zhang)

[*] **Corresponding author:**
Qiangqiang Yuan (yqiang86@gmail.com).
Tingting Liu (ttliu23@whu.edu.cn).

Abstract

Snow cover plays a vital role in the climate system because it is related to climate, hydrological cycle, and ecosystem. On this basis, deriving a long-term and large-scale snow depth (SD) time series and monitoring its temporal and spatial variations are crucial. Passive microwave remote sensing data in combination with in-situ SD data have long been used to retrieve SD. However, the retrieval accuracy is limited in case of sparse meteorological stations, and the high-quality applications of retrieval results are hindered in specific areas. The ground-based global navigation satellite system reflectometry (GNSS-R) method is currently a potential way to monitor SD variations with a high degree of accuracy but has a limited spatial coverage. In this study, a deep learning-based approach, which displays a stronger nonlinear expressiveness capability than conventional neural networks, was applied to estimate SD by combining satellite observations, in-situ data, and GNSS-R estimates. The model was trained and tested with data obtained in Alaska between 2008 and 2017. Results show that the proposed deep belief network model performs better than linear methods and conventional neural network models and demonstrate the effectiveness of combining GNSS-R estimation with increased cross-validation R of 0.85 and decreased RMSE of 15.40 cm. The predicted SD distribution indicates that the variations in mean SD in Alaska for March and April between 2008 and 2017 were associated with the climate anomalies and air temperature. Overall, the proposed deep learning-based method is a promising approach in the satellite-retrieved SD field.

Key words: deep learning, multisource data, GNSS-R, brightness temperature, Alaska, snow depth

1. Introduction

Snow is a crucial component of a climate system and directly affects the energy balance of the Earth's surface due to its heat-insulation effect and high albedo (Che et al. 2016; Dietz et al. 2012; Wu et al. 2018). Snow also plays a prominent role in the water cycle, and snowmelt runoff is a stable and reliable water source in many water-scarce regions (Kang et al. 2014; Shi et al. 2015; Tedesco et al. 2015; Wang et al. 2015). Extensive and continuous snow can also cause natural disasters, such as avalanches, which can lead to considerable loss of life and property. Snow depth (SD) data can provide quantitative information about the material and energy of snow. Thus, obtaining accurate SD information is crucial for the research on climatology and hydrology.

Conventional SD measurement methods can measure SD through in-situ devices with a high degree of accuracy (Rasmussen et al. 2012). However, these methods cannot capture the spatiotemporal SD variation characteristics under sparse distribution of observation stations. Over the past four decades, passive microwave (PM) remote sensing has exhibited the ability to acquire long-term and large-scale SD datasets with the rapid evolution of satellite remote sensing (Armstrong and Brodzik 2002; Liu et al. 2018; Rostosky et al. 2018). PM remote sensing has become an effective way to estimate SD given that it can provide all-day and all-weather monitoring and spatially continuous information of SD variation with high temporal resolution (Gu et al. 2014; Li et al. 2019).

PM remote sensing observation is based on the assumption that the electromagnetic

81 radiation characteristics of snow have a strong dependence on SD (Rosenfeld and
82 Grody 2000). In snow-covered areas, the microwave radiometer carried by a satellite
83 records the microwave radiation energy from the ground in the form of brightness
84 temperature (Tb), which includes two main components: one is the radiation from the
85 snow cover, and the other is that from the ground beneath. The brightness temperature
86 decreases with the increase in SD because of the volume scattering of snow particles
87 (Dai et al. 2012; Mashtayeva et al. 2016). The scattering effect is directly proportional
88 to the microwave frequency; thus, the brightness temperature of the high-frequency
89 channel is lower than that of the low-frequency channel (Shi et al. 2016; Ulaby and
90 Stiles 1980). Therefore, SD retrieval based on PM remote sensing is often to establish
91 the functional relationship between SD and brightness temperature.

92 Several algorithms have been developed to estimate SD by combining remote
93 sensing data and station observations. The most common method is to establish the
94 linear relationship between SD and brightness temperature by utilizing the difference
95 between the horizontally polarized brightness temperatures of 19 and 37 GHz and the
96 ground-measured SD. In many studies, Chang algorithm (Chang et al. 1987) has been
97 modified by considering the parameters that affect the SD retrieval accuracy, such as
98 forest and terrain (Foster et al. 1997; Langlois et al. 2011). However, linear methods
99 cannot exactly describe the nonlinear relationship between SD and brightness
100 temperature and tend to underestimate SD (Gan et al. 2013). Therefore, nonlinear
101 methods, such as artificial neural networks (ANNs), have emerged to establish the
102 nonlinear relationship between the input variables (brightness temperature and

auxiliary data) and SD. For instance, ANNs have been trained to retrieve SD by combining in-situ measurements and brightness temperatures observed by using PM sensors (Cao et al. 2008; Santi et al. 2012; Tabari et al. 2010; Tedesco et al. 2004). ANNs have also been trained with model simulations for the estimation of SD (Chang and Tsang 1992; Davis et al. 1993; Tedesco et al. 2004). Brightness temperatures are simulated on the basis of radiative transfer model by using some snow properties, and the simulated brightness temperature and SD are taken as the input and output of ANN models, respectively. Moreover, some auxiliary parameters (e.g., forest cover fraction, and elevation) have been regarded as input parameters of ANN models to improve the retrieval accuracy under the influence of forest and terrain (Bair et al. 2018; Evora et al. 2008; Gan et al. 2009). Santi et al. (2014) used AMSR-E equivalent brightness temperature corrected for the effects of orography and forest coverage instead of the original brightness temperature as inputs of ANN model to estimate SD and demonstrated the improvement of retrieval accuracy. These nonlinear methods have shown great advantages in estimating SD and have higher precision than linear methods.

The ground-based global navigation satellite system reflectometry (GNSS-R) method is currently a new way of monitoring SD variation at the spatial scale of approximately 1000 m^2, which is larger than the spatial scale of in-situ measurements, with high temporal and spatial resolution. Larson et al. (2009) first estimated SD on the basis of signal-to-noise ratio (SNR) because the multipath reflection component of the SNR observations is associated with SD. The reliability and accuracy of the

SNR-based method have been proven at sites with three land cover types (Nievinski and Larson 2014). Tabibi et al. (2017) analyzed the SD estimated using different frequency bands of global positioning system (GPS) and GLONASS and found that accurate results can be obtained using GPS L2C and GLONASS SNR observations. The solutions of SD measurement in different interference environments have been proposed to address the signal interference problem of SNR-based methods in complex terrain environment by analyzing the interference factors (Vey et al. 2016; Zhang et al. 2017). A GNSS-R network (PBO H2O network) based on GNSS stations has also been developed on the western coast of the USA and Alaska (Larson and Nievinski 2013), where GNSS-R SD is directly available through open access. The accuracy of the GNSS-R SD product has been validated and has shown a precision of a few centimeters (Larson and Nievinski 2013; McCreight et al. 2014). The GNSS-R product from PBO H2O network has been used as the true value of SD to validate other SD products (Boniface et al. 2015). In summary, the GNSS-R method not only can monitor SD with the advantage of an all-day and all-weather ability but also can estimate SD with a high degree of accuracy. However, GNSS-R observation is also restricted to a limited spatial scale, and GNSS-R stations are sparsely distributed.

Deep learning, which displays a stronger nonlinear expressiveness capability than conventional neural networks, has achieved great success in geoscience inversion, including fine particulate matter (Li et al. 2017) and soil moisture (Jia et al. 2019; Song et al. 2016). However, deep learning has rarely been applied to retrieve SD to date. Thus, this study aimed to establish a deep learning-based model for estimating

147 SD. However, the sparsely distributed samples from combining only satellite and
148 sparsely distributed in-situ observations may limit the accuracy of SD retrieval. In this
149 study, the SDs estimated by the GNSS-R method were taken as true values and
150 combined with in-situ observations to increase the station density of the sample data
151 for the following two reasons: one is that the accuracy of the GNSS-R method in SD
152 retrieval is high, and the other is that the spatial scale of the GNSS-R technique
153 (nearly 1000 m^2) is better than the point-scale (<1 m^2) in-situ measurements (Xu et al.
154 2018) in terms of brightness temperature data. Therefore, the proposed deep
155 learning-based SD retrieval model was constructed and evaluated on the basis of the
156 combination of satellite observations, in-situ data, and GNSS-R estimation. Alaska
157 was selected as the study region because it has an abundance of snow and has a
158 mature GNSS-R SD product that is available through open access by connecting to
159 the PBO H2O network.

160 The remainder of the paper is organized as follows. In Section 2, the study region
161 and data used are described. Section 3 introduces the deep learning-based SD retrieval
162 method, that is, the deep belief network (DBN) model developed here, and the
163 indicators used for the evaluation. In Section 4, the performance evaluation of this
164 model against daily ground-measured SD data are described, and we compare the
165 results with those of four other SD retrieval models, namely, Chang, multiple linear
166 regression (MLR), back propagation neural network (BPNN), and generalized
167 regression neural network (GRNN). The former two are linear models, and the latter
168 two are nonlinear ones. On the basis of the derived SD distribution from 2008 to 2017,

we analyze the variation in SD in Alaska over this time period and its response to climate anomalies and air temperature. Finally, our work is summarized in Section 5.

2. Study region and data

2.1. Study region

Alaska, which is in the latitude and longitude range of 54°N–71°N and 130°W–173°W, was chosen as the study region (Fig. 1). The study period was from 2008 to 2017. Alaska is located at high latitudes. Thus, most parts of this region are cold all year round. Alaska experiences abundant precipitation as a result of being surrounded by three oceans (the North Pacific Ocean, the Bering Sea, and the Arctic Ocean). Therefore, this region has an abundance of snow cover. Typically, north Alaska has a polar cold and dry climate with the air temperature below zero all year round. Central Alaska has a continental climate with an average annual temperature of −2.47 °C and an average annual precipitation of 275 mm at Fairbanks, while southern Alaska has a temperate maritime climate with an average temperature of 3.7 °C and an average annual precipitation of 617 mm at Homer. Mature GNSS-R SD products, as well as conventional in-situ and satellite observations, are available in Alaska. The above-mentioned considerations indicate that Alaska is ideal for the research on snow cover using integrated multi-source data.

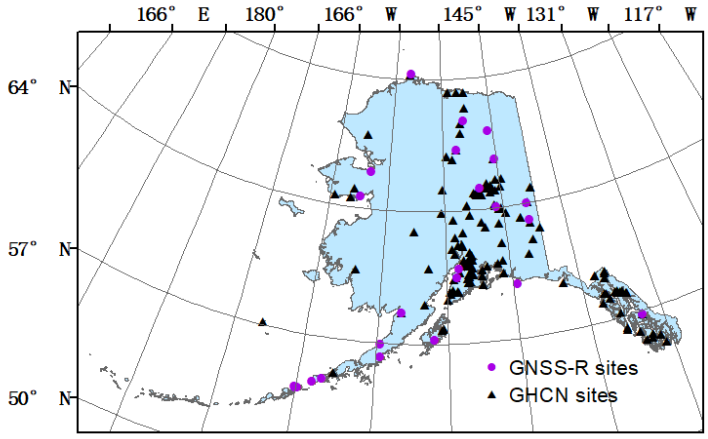

Fig. 1. Study area and the distribution of Global Historical Climate Network (GHCN) and Global Navigation Satellite System Reflectometry (GNSS-R) stations. The blue area represents the region of Alaska.

2.2. Data

2.2.1 Satellite observations

The Special Sensor Microwave Imager/Sounder (SSMIS) is a satellite-borne microwave radiometer onboard the U.S. Defense Meteorological Satellite Program F17. The brightness temperature data observed by SSMIS gridded to the EASE-Grid with daily temporal resolution and 25 km spatial resolution (Armstrong et al. 1994; Brodzik 2002) have been available at the National Snow and Ice Data Center (https://nsidc.org/) since December 2006 and contain four frequencies, namely, 19, 22, 37, and 91 GHz. Except for 22 GHz, which is only vertically polarized (i.e., Tb22V), the other frequencies have horizontal and vertical polarization modes (i.e., Tb19H, Tb19V, Tb37H, Tb37V, Tb91H, and Tb91V.). Thus, seven channels of brightness temperature are available. The daily SSMIS brightness temperature data from 2008 to 2017 were downloaded from the National Snow and Ice Data Center. In this study,

204 descending overpass observations (during early morning) were used given that liquid
205 water could be existing in the snow during the afternoon satellite overpass and the SD
206 could not be retrieved in the case of wet snow (Che et al. 2008; Kelly and Chang
207 2003).

208 **2.2.2 In-situ SD**

209 The Global Historical Climate Network (GHCN, https://www.ncdc.noaa.
210 gov/snow-and-ice/) integrates daily climate datasets from meteorological stations
211 around the world and provides in-situ SD datasets for daily temporal resolution. The
212 daily SD datasets include the information of location, measuring time, and SD. Daily
213 in-situ SD data of 155 sites within the study region from 2008 to 2017 were obtained
214 from GHCN and utilized for the construction and performance evaluation of the SD
215 retrieval model (Tsutsui and Maeda 2017).

216 **2.2.3 GNSS-R estimation**

217 The daily GNSS-R SD product data can be obtained from the PBO H2O Data
218 Portal (https://gnssh2o.jpl.nasa.gov/index.php?product=snow), which uses a
219 traditional geodetic GPS signal-receiving station to monitor the change in SNR for
220 long time series and then estimates the SD based on GNSS-R with a high precision of
221 a few centimeters (Larson et al. 2009; Larson and Nievinski 2013). A total of 25
222 GNSS-R stations are present in Alaska (Fig. 1), and the daily GNSS-R SD data from
223 2008 to 2017 were taken as the actual SD, together with the in-situ measurements, to
224 establish and evaluate the SD retrieval model.

2.2.4 Forest cover fraction data

Forest cover fraction data were also used considering the potential impact of forest on SD retrieval. The MOD44B Version 6 Vegetation Continuous Fields (VCF) product is a global representation of surface vegetation cover that can continuously and quantitatively portray land-surface cover at a pixel resolution of 250 m. Forest cover fraction data (Fig. 2) were obtained from the MOD44B MODIS/Terra VCF Yearly L3 Global 250 m SIN Grid V006 product (https://ladsweb.modaps.eosdis.nasa.gov/ search/order/1/MOD44B--6).

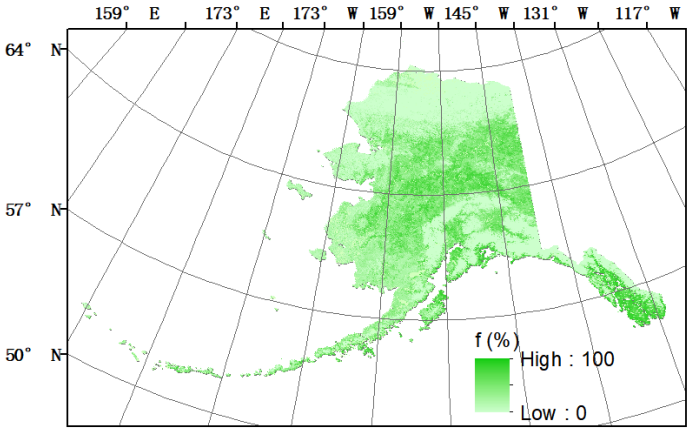

Fig. 2. Distribution of the forest cover fraction for 2008 as an example.

2.2.5 Topographic data

Elevation parameter was utilized as auxiliary data to consider the effect of topographic parameters on the SD retrieval accuracy. The ETOPO1 Global Relief Model was used as elevation data, and its spatial resolution is 1 arc minute or approximately 2 km (Amante and Eakins 2009). These model data (Fig. 3) can be downloaded from http://www.Ngdc.noaa.gov/mgg/global/.

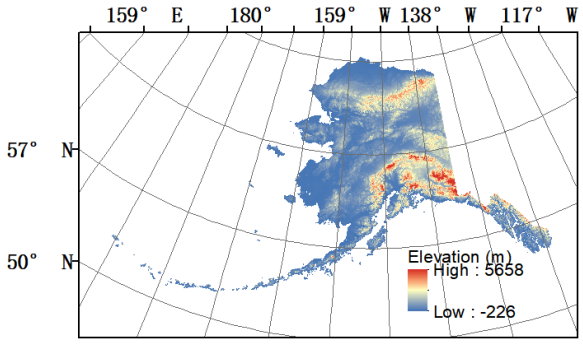

Fig. 3. Elevation variation in Alaska.

2.3. Data matching and processing

First, the elevation and forest cover fraction data were regridded to the EASE-Grid, and the mean values of the forest cover fraction and elevation were calculated for the corresponding EASE-Grid to match the brightness temperature data. In addition, the SD data from multiple in-situ and GNSS-R stations were averaged for each EASE-Grid. Then, SD measurements from GHCN and PBO H2O network were associated with the satellite observations and ancillary data.

Second, we applied Grody's decision tree method (Che et al. 2008; Grody and Basist 1996) to distinguish snow from other scattering signals given the resemblance of the microwave radiation characteristic of snow to that of frozen ground, cold desert, and precipitation (Table 1).

Table 1. Conditions for removing other scattering signatures.

Steps	Conditions
Scattering signature	Tb19V-Tb37V>0K
Precipitation	Tb22V>258K or 258K≥Tb22V≥254K and Tb19V-Tb37V≤2K
Cold deserts	Tb19V-Tb19H≥18K and Tb19V-Tb37V≤10K
Frozen ground	Tb19V-Tb19H≥8K and Tb19V-Tb37V≤2K

Considering the hindering effect of wet snow on the SD retrieval based on PM remote sensing, the following dry snow criteria (Singh and Gan 2000; Xiao et al. 2018) were applied to remove wet snow for ensuring high accuracy of SD retrieval:

$$\begin{aligned} &\mathrm{Tb37V} < 250K \\ &\mathrm{Tb19V} - \mathrm{Tb37V} \geq 9\mathrm{K} \\ &\mathrm{Tb37V} - \mathrm{Tb37H} \geq 10\mathrm{K} \\ &P_{factor} = \frac{Tb37V - Tb37H}{Tb37V + Tb37H}, P_{factor} > 0.026 \end{aligned} \quad (1)$$

Following the above-mentioned steps, wet snow and other scattering signals were excluded, and 11,447 dry snow samples were identified.

3. Methodology

3.1. Structure of the DBN model

The DBN model proposed in 2006 is a typical deep learning model (Hinton et al. 2006). The model can be utilized to solve prediction and classification problems (Chen et al. 2015; Huang et al. 2014). Consequently, the SD retrieval model in this study was established on the basis of DBN model.

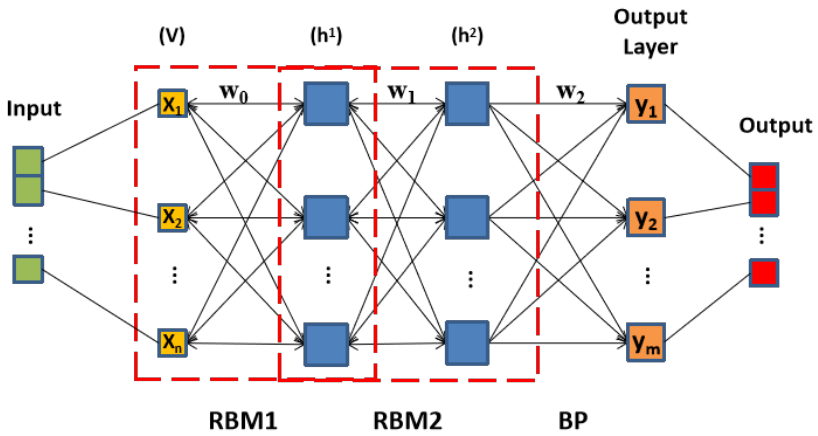

Fig. 4. Structure of the DBN model.

The DBN model is composed of a back propagation (BP) layer and several restricted Boltzmann machine (RBM) layers. For instance, Fig. 4 shows the structure of a DBN model with two RBM layers. An RBM is made up of a visible layer (v) used to input training data and a hidden layer (h) used to extract data features, with the visible and hidden layers being bidirectionally linked. The first RBM's hidden layer is the second RBM's visible layer.

The training process for a DBN model consists of two main steps. The first step is to train the RBMs. When data are transmitted from v to h in the first RBM, the opening probability of every neuron in the hidden layer can be calculated according to Eq. (2):

$$p(h_j = 1|v) = \sigma(\sum_{i=1}^{m} \omega_{ij} v_i + c_j) \tag{2}$$

where i and j respectively indicate the number of the ith visible neuron and the jth hidden neuron. ω_{ij} denotes the weight between visible neuron i and hidden neuron j, while c_j refers to the bias of the jth hidden neuron. Sigmoid function σ ( ) acts as the transfer function.

The calculated opening probability of each hidden neuron is compared with the random value μ extracted from the 0,1 uniform distribution, and the hidden neurons are updated to 0 or 1 in accordance with Eq. (3):

$$h_j = \begin{cases} 1, p(h_j = 1|v) \geq \mu \\ 0, p(h_j = 1|v) < \mu \end{cases} \quad \mu \sim U\,(0,1) \tag{3}$$

So is the calculation process from hidden layer to visible layer. In general, the contrastive divergence algorithm (Hinton and Salakhutdinov 2006) is utilized to train an RBM. The neurons' weights and bias are then updated as the following formula until v is approximately equal to $v1$:

$$\omega = \omega + \varepsilon \cdot ((h)^T v - (h1)^T v1)$$
$$b = b + \varepsilon \cdot (v - v1) \quad (4)$$
$$c = c + \varepsilon \cdot ((h)^T v - (h1)^T v1)$$

where ε refers to the learning rate; h, $h1$ are obtained from v, $v1$ using Eqs. (2) and (3); $v1$ is reconstructed from the hidden layer (h); and b and c respectively indicate the bias for the visible and hidden neurons.

The RBMs are pretrained one after another without supervision, and the weights obtained through this unsupervised pretraining are used to initialize the multilayer network. The second step of the training process of the DBN is to fine-tune the coefficients between layers using a supervised BP algorithm.

3.2. SD retrieval model based on a DBN

In our case, the DBN model is adopted to learn the relationship between the input variables and SD through learning from the sample datasets:

$$SD = g(Tb19H, Tb19V, Tb37H, Tb37V, lat, lon, elevation, f, time) \quad (5)$$

where $g()$ means the estimation function; lat, lon, and $elevation$ represent 3D localization; and f indicates the forest cover fraction.

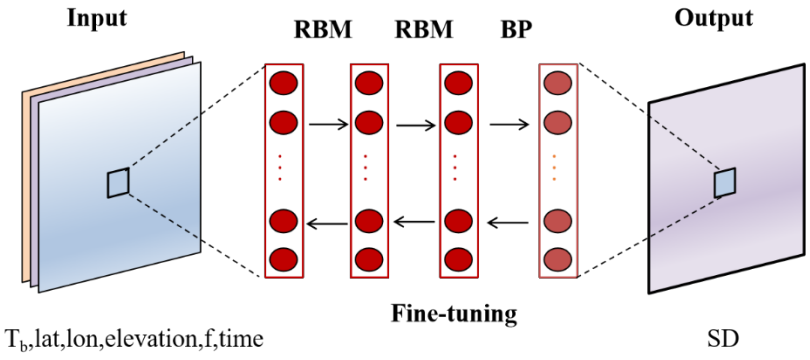

Fig. 5. Structure of the DBN model for SD modeling.

Figure 5 shows the schematic of the DBN model used to retrieve SD. The input variables are PM horizontal and vertical polarization brightness temperatures of

19 and 37 GHz, latitude, longitude, elevation, forest cover fraction, and time. We apply two hidden layers (two RBMs), where the amount of neurons in every hidden layer is 16. Following the two RBMs is a BP layer with one neuron (SD).

The specific process of the DBN model for SD modeling consists of three steps, as shown in Fig. 6.

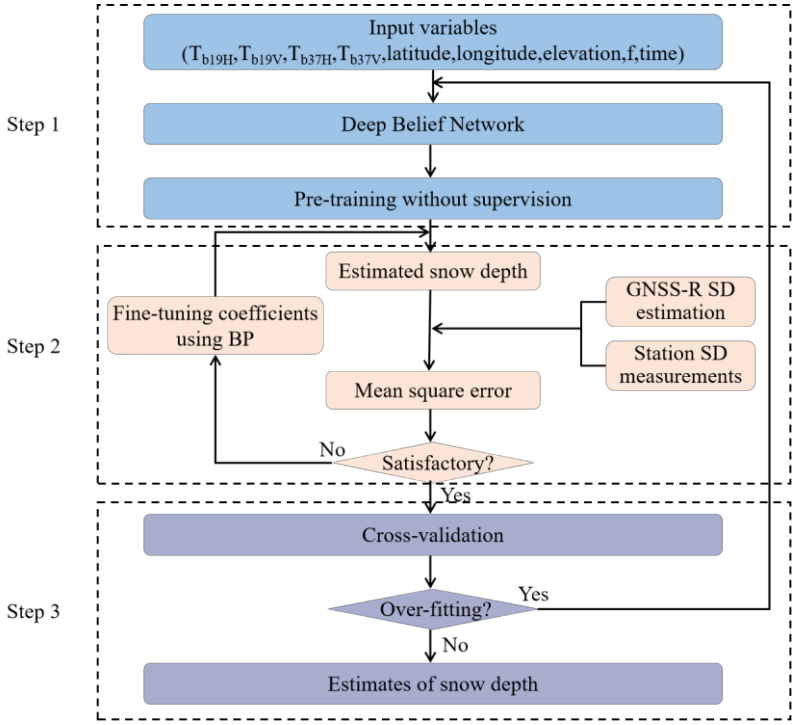

Fig. 6. Flowchart of the DBN model for SD modeling.

First, the variables of horizontal and vertical polarimetric brightness temperatures of 19 and 37 GHz, latitude, longitude, elevation, forest cover fraction, and time are input into the model. In this step, only the input data are used to pretrain the DBN model, which indicates that the initial coefficients of this model are trained from input data. Meanwhile, actual SD is not utilized for tuning the coefficients in such process.

Second, we can estimate the SD value from the DBN model. Subsequently, the mean-square error (MSE) between the actual and retrieved SD is calculated and returned to fine-tune the coefficients of the model by utilizing the BP algorithm

328 (Rumelhart et al. 1988). This procedure is repeated until the DBN model achieves a
329 satisfactory performance. Then, the relationship between SD and satellite brightness
330 temperature can be effectively established through this step.

331 Finally, this model is validated and then applied to estimate the SD where no ground
332 stations exist. Accordingly, we can acquire the spatially continuous distribution of the
333 SD.

334 We used three statistical indicators, namely, the correlation coefficient (R), the mean
335 absolute error (MAE, cm), and the root-mean-square error (RMSE, cm), to
336 quantitatively evaluate the model performance. We adopted a 10-fold cross-validation
337 technique to test the over-fitting and predictive power of the model (Rodriguez et al.
338 2010). All the sample data were divided into 10 subsets equally and randomly. One of
339 the subsets was selected as validation samples in turn, while the others were utilized
340 for model fitting. Then, 10 results were averaged to evaluate the performance of the
341 DBN model. Small differences between the model fitting and cross-validation
342 statistics suggest non-overfitting (Hu et al. 2013). In addition, among the 10 models,
343 the one which performed best, with the highest validation R, the lowest validation
344 MAE, and the lowest validation RMSE, was selected to retrieve SD over the whole of
345 Alaska.

346 **3.3. Other SD retrieval algorithms for comparison**

347 BPNN (Rumelhart et al. 1988; Tedesco et al. 2004), GRNN (Specht 1991), Chang
348 algorithm (Chang et al. 1987), and MLR (Xiao et al. 2018) were utilized to construct
349 SD retrieval models on the basis of the same samples used by the DBN model for
350 better assessing the performance of the deep learning-based SD retrieval model. The
351 performances of these methods were compared with those of the DBN model.

3.3.1. Linear methods

Chang algorithm is a linear method used to estimate SD through performing linear regression for the difference in the brightness temperature using 18 and 36 GHz horizontal polarization and SD.

$$SD = 1.59 * (Tb18H - Tb36H) \quad (6)$$

where SD is estimated in centimeters. Tb18H and Tb36H denote the horizontal polarization brightness temperatures of 18 and 36 GHz, which were replaced with SSMIS horizontal polarization brightness temperatures of 19 and 37 GHz in this study (Xiao et al. 2018).

In addition, an SD retrieval model based on the MLR method was established using nine parameters (the same as the DBN model) for predicting SD.

$$SD = \alpha_0 + \alpha_1 \cdot lat + \alpha_2 \cdot lon + \alpha_3 \cdot elevation + \alpha_4 \cdot Tb19H + \alpha_5 \cdot Tb19V$$
$$+\alpha_6 \cdot Tb37H + \alpha_7 \cdot Tb37V + \alpha_8 \cdot f + \alpha_9 \cdot time \quad (7)$$

3.3.2. Nonlinear method

As with the DBN model, BPNN and GRNN are data-driven learning models. The same input and output parameters were again used in the two neural networks. However, the BPNN model (Fig. 7a) has a relatively simple structure with three layers (input, hidden, and output layers), and the GRNN model (Fig. 7b) uses several hidden layer neurons to achieve function approximation. Instead, the DBN model not only has a more complex structure but also initializes through unsupervised pretraining.

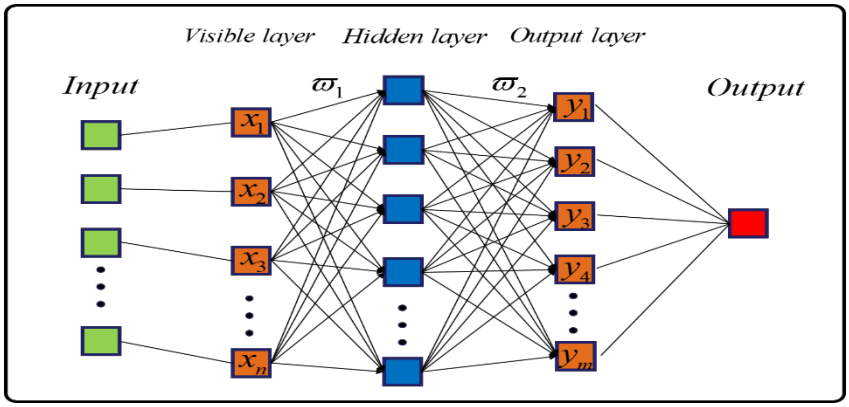

(a) BPNN

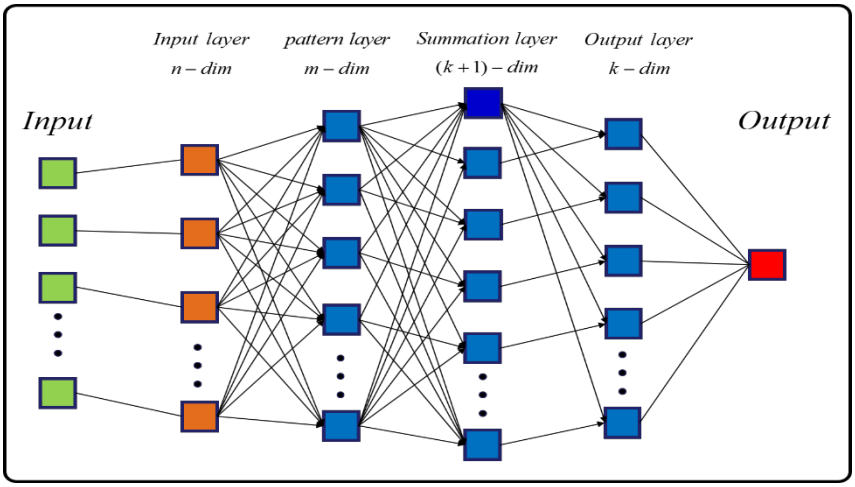

(b) GRNN

Fig. 7. Structure of the (a) BPNN model and (b) GRNN model.

4. Results and analysis

4.1. Evaluation of model performance

4.1.1. Performance of DBN modeling

Primarily, remote sensing data, auxiliary data, and in-situ observations were integrated to generate the sample datasets for the DBN model and the four alternative methods mentioned above. As presented in Table 2, the two kinds of linear methods, namely, Chang algorithm and the MLR method, perform the worst (cross-validation R of 0.15/0.47, MAE of 22.33/19.12 cm, and RMSE of 35.36/26.91 cm) as expected owing to that the nonlinear relationship between SD and brightness temperature is described as linear. In consideration of the nonlinear relationship between the input

382 variables and SD, BPNN and GRNN perform better than the linear models
383 (cross-validation R of 0.78/0.68, MAE of 12.80/15.17 cm, and RMSE of
384 19.01/22.33 cm). The DBN model, which is a complex learning model, can better fit
385 the nonlinear relationship and obtains the best performance (cross-validation R of 0.81,
386 MAE of 11.15 cm, and RMSE of 17.96 cm) among the other models.

387 Fig. 8 presents the scatter plots of actual SD and estimated value retrieved by the five
388 algorithms. The underestimates and overestimates of SD retrieved by the DBN model
389 are less than those of the GRNN and BPNN models, as presented in Figs. 8e, c, and d.
390 These results demonstrate that the proposed deep learning-based SD retrieval model
391 with a more complicated structure and a layer-by-layer unsupervised pretraining
392 technique can estimate SD with a higher degree of accuracy. The two linear methods, as
393 shown in Figs. 8a and b, tend to underestimate SD when the actual SD value exceeds
394 50 cm. This phenomenon can be due to the saturation of the difference in the brightness
395 temperature. The results of MLR are better than those of Chang algorithm. This result
396 may be due to that more parameters that correspond to snow properties are used in
397 MLR.

398 **Table 2.** Model fitting and cross-validation performance of the models.

Method	Model fitting			Cross-validation		
	R	MAE	RMSE	R	MAE	RMSE
Chang				**0.15**	**22.33**	**35.36**
MLR	**0.47**	**19.15**	**26.94**	**0.47**	**19.12**	**26.91**
GRNN	**0.70**	**14.67**	**21.60**	**0.68**	**15.17**	**22.33**
BPNN	**0.81**	**11.56**	**18.05**	**0.78**	**12.80**	**19.01**
DBN	**0.83**	**10.16**	**17.18**	**0.81**	**11.15**	**17.96**

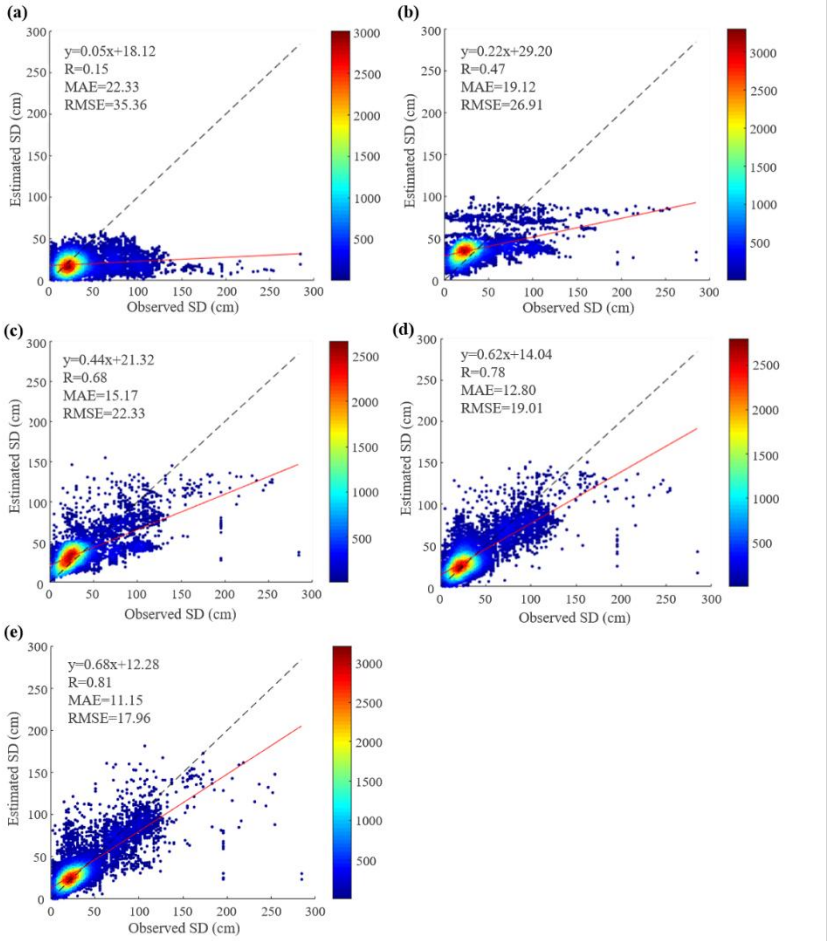

Fig. 8. Scatter plots of the cross-validation results of the five algorithms: (a) Chang; (b) MLR; (c) GRNN; (d) BPNN; (e) DBN.

The SD retrieval models in this section were established without combining the high-precision GNSS-R estimates. Thus, we used high-precision GNSS-R estimates as independent evaluation data to validate the retrieval accuracy of the DBN model and four other models for further verifying whether the DBN model performs best among the five compared methods. Fig. 9 shows the scatter plots of GNSS-R SD and estimated values retrieved by the five algorithms. The performances of the two linear methods remain the worst (validation R of 0.45/0.56). Although the MLR method can consider more parameters, it cannot map the complex nonlinear relationship between input parameters and SD. On the contrary, GRNN and BPNN can fit this nonlinear relationship and perform better than linear methods with validation R of 0.64/0.69.

Furthermore, the DBN model remains the best-performing model with validation R of 0.76 given its stronger ability for nonlinear mapping.

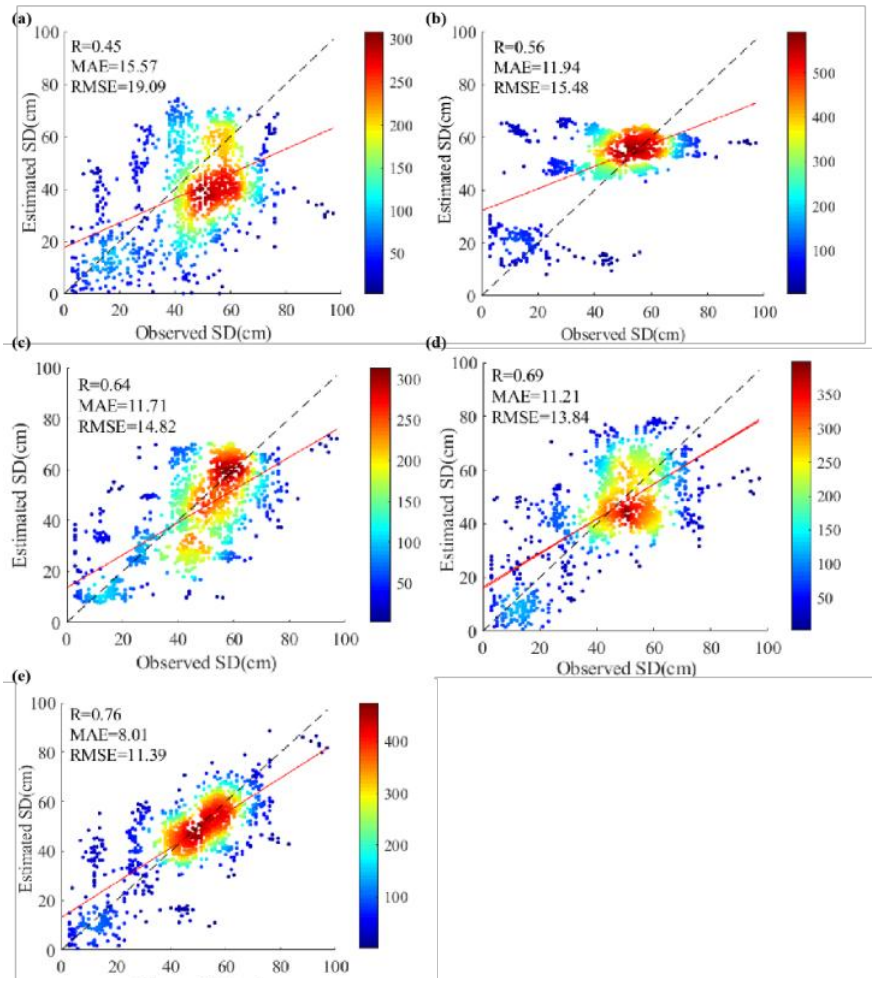

Fig. 9. Scatter plots of the validation results of the five algorithms by using GNSS-R data as independent evaluation data:(a) Chang; (b) MLR; (c) GRNN; (d) BPNN; (e) DBN.

In summary, the nonlinear methods (BPNN, GRNN, and DBN) are superior to the linear methods, while the proposed DBN SD retrieval model performs the best among all compared models.

4.1.2. Effect of the added GNSS-R SD estimation

In this study, GNSS-R SD estimates were taken as the actual SD, together with the in-situ SD data, to increase the station density of the sample data. We compared the results of the models combining satellite observations, in-situ observations, and GNSS-R estimates with those of SD retrieval models combining only satellite

observations and in-situ observations, as described in Section 4.1.1, to prove the effect of the addition of GNSS-R estimates.

Table 3 lists the accuracy of the five SD retrieval models combining satellite observations, in-situ observations, and GNSS-R estimates. Fig. 10 presents the scatter plots of the actual SD value and the estimated SD retrieved by the five algorithms. The DBN SD retrieval model and the four models based on combining satellite observations, in-situ observations, and GNSS-R estimates all show higher accuracy in estimating SD than the SD retrieval models based on combining satellite observations and in-situ observations. This result demonstrates that considering the GNSS-R SD estimates to increase the density of the sample data contributes to improving the SD retrieval accuracy. The DBN model also performs best when GNSS-R SD estimates are considered to increase the station density of the sample data. This model has cross-validation R of 0.85, MAE of 9.55 cm, and RMSE of 15.40 cm.

Table 3. Model fitting and cross-validation performance of the models.

Method	Model fitting			Cross-validation		
	R	MAE	RMSE	R	MAE	RMSE
Chang（+GNSS-R）				**0.20**	**21.34**	**33.52**
MLR（+GNSS-R）	**0.48**	**17.98**	**25.68**	**0.48**	**17.99**	**25.66**
GRNN（+GNSS-R）	**0.75**	**12.44**	**19.08**	**0.72**	**13.25**	**20.26**
BPNN（+GNSS-R）	**0.83**	**10.33**	**16.42**	**0.80**	**11.35**	**17.42**
DBN (+GNSS-R)	**0.87**	**8.80**	**14.39**	**0.85**	**9.55**	**15.40**

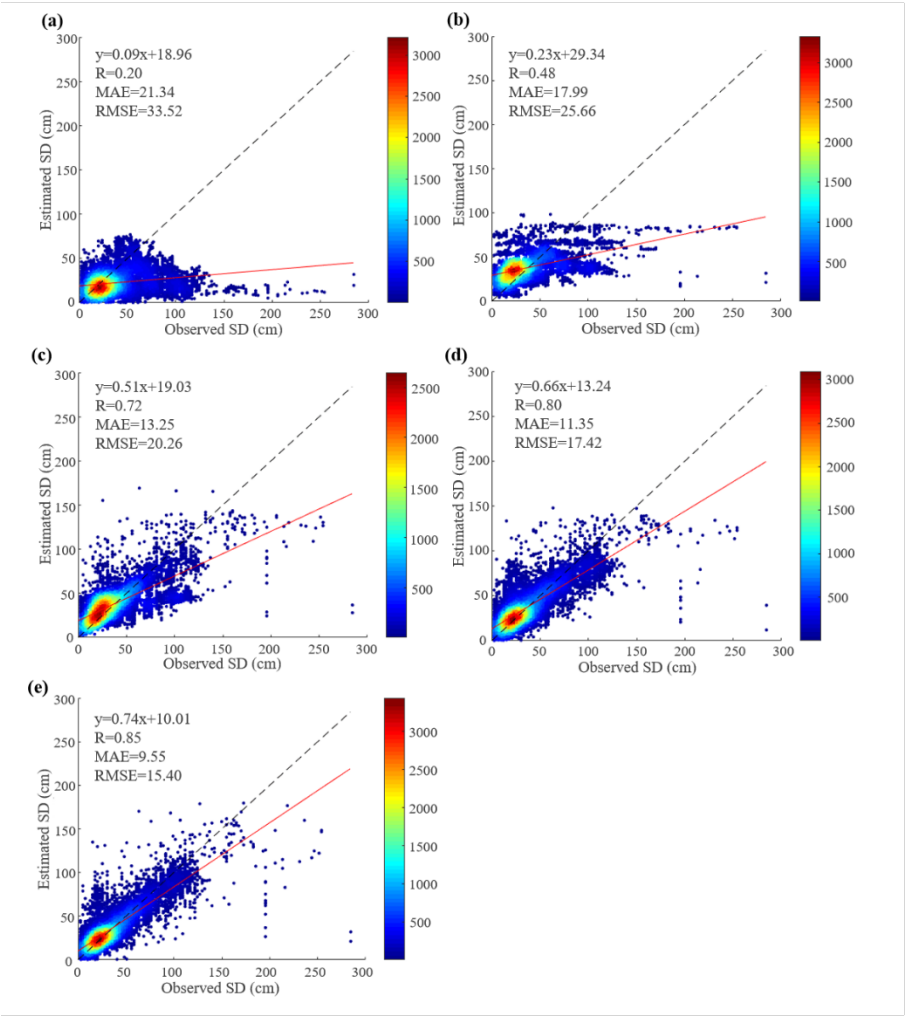

Fig. 10. Scatter plots of the cross-validation results of the five algorithms: (a) Chang; (b) MLR; (c) GRNN; (d) BPNN; (e) DBN.

4.2. Analysis of variations in SD in Alaska

Based on the proposed DBN SD retrieval model described in Section 4.1.2, the variables of longitude, latitude, elevation, brightness temperature of four channels, the forest cover fraction of each grid cell in Alaska, and time were taken as input data. The daily SD in Alaska from 2008 to 2017 was finally predicted.

Snow in Alaska is relatively stable from March to April when the SD value nearly reaches the maximum value in a year (Liu et al. 2013). Thus, the mean SD from March to April each year was calculated to analyze the variation in average SD for March and April from 2008 to 2017.

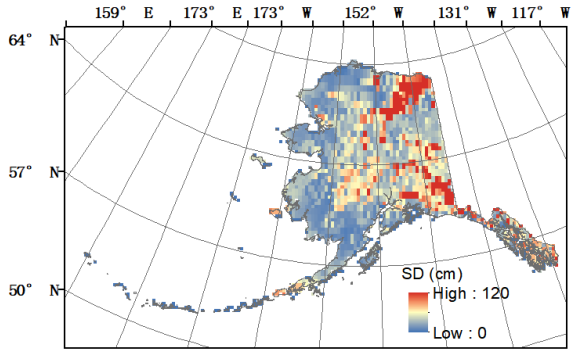

Fig. 11. Distribution of the average SD for March and April in 2008 over Alaska.

Taking the SD distribution maps of Alaska in 2008 as an example (Fig .11), it can be seen that the snow of Alaska presents certain spatial distribution characteristics and significant regional differences. The north of Alaska has the greatest SD. This condition may be due to the cold and sub-temperate continental climate of this region. Meanwhile, the overall climate of this region is humid but cold because of its low terrain and closeness to the Arctic Sea. In addition, the average SD in the inland regions is greater than that in the southwest part of Alaska.

The SD anomalies for March and April each year were calculated by subtracting the overall average SD for March and April in this decade (Fig .12). Red represents an increase in SD, while blue represents a decrease in SD. We can find that from 2011 to 2013, as well as 2009 and 2017, SD anomalies manifest as increase in most area of Alaska, especially in southwest Alaska. In addition, the increase in SD over Alaska was most apparent in 2012. On the contrary, SD anomalies manifest as decrease in most areas of Alaska from 2014 to 2016, as well as 2010.

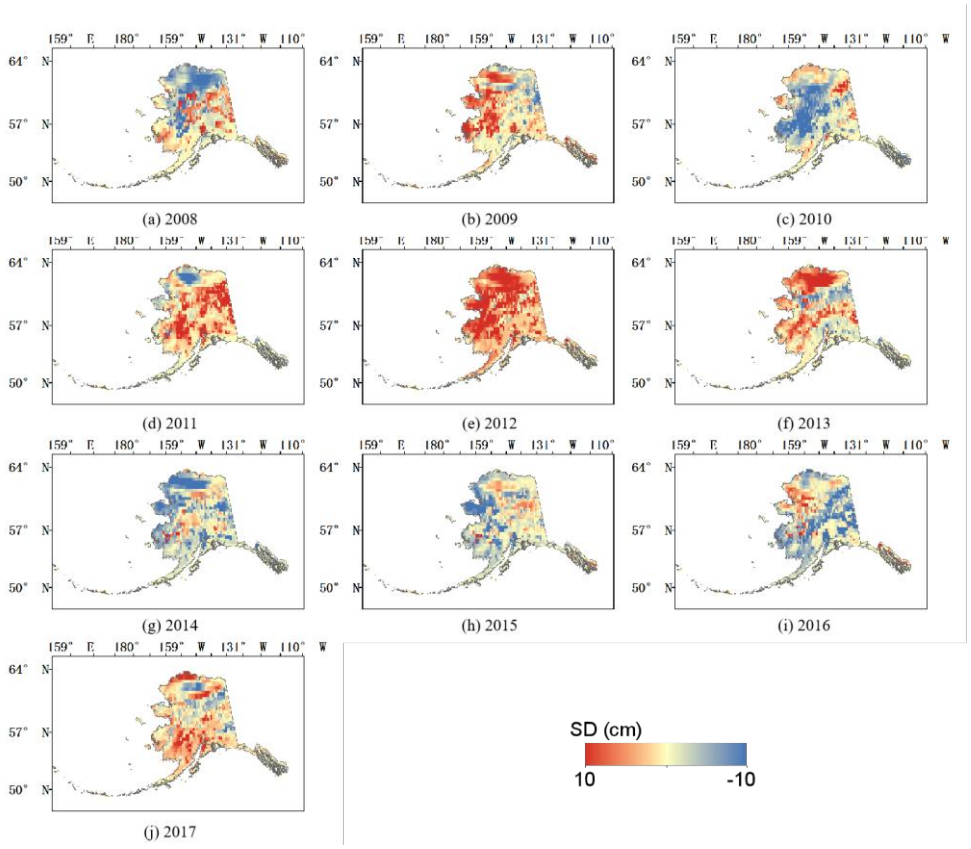

Fig. 12. SD anomalies for March and April each year from 2008 to 2017.

In the context of global warming, climate anomalies such as El Niño and La Niña would intensify (Ham 2018). The change in SD during the decade may be a response to the change in temperature and climate anomalies. El Niño occurs when water temperatures in the equatorial sea area of the eastern and central Pacific Ocean continue to warm abnormally, which causes a corresponding change in the global climate. La Niña is the opposite of El Niño and often follows it. El Niño and La Niña greatly influence global climate. Fig. 13a presents the El Niño/Southern Oscillation (ENSO) intensities in the multivariate ENSO index (MEI) during this period, which are available at www.esrl.noaa.gov/psd/enso/mei/table.html. Positive MEI values denote El Niño, while negative MEI values indicate La Niña (Wang et al. 2018). Then, the SD anomalies in Fig.12 were averaged over Alaska for each year and plotted with

the ENSO intensities in Fig. 13a. Comparing the change in SD with the occurrence of these climate anomalies (Fig.13a), we can find that the changes in SD in Alaska have been generally consistent with the climate anomalies over the past decade. From 2008 to 2009 and from 2011 to 2013, as well as 2017, La Niña occurred in March and April, and the SD increased correspondingly. By contrast, from 2014 to 2016, as well as 2010, El Niño occurred, and the SD decreased correspondingly.

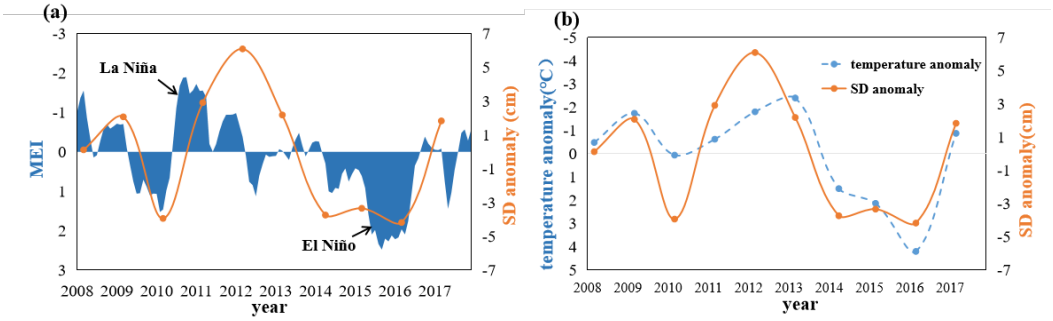

Fig. 13. ENSO intensities in MEI, mean SD anomaly, and mean air temperature anomaly for March and April from 2008 to 2017. (a) ENSO intensities in MEI and mean SD anomaly for March and April from 2008 to 2017. (b) Mean SD anomaly and mean air temperature anomaly for March and April from 2008 to 2017.

The degree of SD change is not completely proportional to the intensity of climate anomalies, especially in 2012, 2013, and 2017. The change in SD may be also related to air temperature, except for the climate anomalies. Air temperature data from NOAA GHCN_CAMS Land Temperature Analysis (https://www.esrl.noaa.gov/psd/data/) were used. The air temperature anomalies for March and April each year in this decade were averaged over Alaska and shown with the mean SD anomalies in Fig. 13b. We can find that in 2013, La Niña was weak, and correspondingly, the increase in SD anomalies should be small. However, the significant decrease in air temperature in 2013 resulted in a larger increase in SD. The case in 2017 is also similar to that in 2013. Besides, the La Niña phenomenon was stronger in 2011 than in 2012, but due to

the air temperature was lower in 2012, resulting in the SD in 2012 larger than that in 2011. Therefore, the change in SD is mainly affected by the combination of the change in temperature and climate anomalies. In addition to the influence of climate anomalies and temperature, some other factors that may affect the change in SD, such as ocean currents and terrain, etc., require further discussion.

5. Conclusions

In this study, we innovatively introduced a deep learning network to improve the precision of satellite-derived SD. In addition, high-precision GNSS-R SD product data were utilized as the actual value of the SD, together with ground-measured SD data, to increase the station density of the sample data. The results show that the DBN SD retrieval model estimates SD more accurately than linear methods and conventional neural network models. Furthermore, the effectiveness of combining GNSS-R estimates for increasing the station density of the sample data was demonstrated. Specifically, R increases from 0.81 to 0.85, MAE decreases from 11.15 cm to 9.55 cm, and RMSE decreases from 17.96 cm to 15.40 cm. Finally, the daily SD over the whole of Alaska was predicted using the proposed DBN SD retrieval model. The results display that the variation in SD for March and April between 2008 and 2017 in Alaska is mainly associated with the occurrence of climate anomalies and the change in air temperature over this time period.

There is still room for improvement of the proposed approach and for further study. On the one hand, the current spatial resolution of estimated SD is coarse (25 km × 25 km), which would limit its application in operational hydrological modeling and snow-caused disaster monitoring. Thus, enhancing the spatial resolution of the SD data is required. On the other hand, we only applied a deep learning network (the

529 DBN model) to establish the relationship between brightness temperature and SD.
530 Whether other deep learning models can better handle this issue is worth
531 investigating.

532 **References**

533 Amante, C., & Eakins, B.W. (2009). ETOPO1 arc-minute global relief model:
534 procedures, data sources and analysis
535
536 Armstrong, R., Knowles, K., Brodzik, M., & Hardman, M. (1994). DMSP
537 SSM/I-SSMIS pathfinder daily EASE-grid brightness temperatures. Version 2. *NASA*
538 *National Snow Ice Data Center Distributed Active Archive Center: Boulder, CO, USA*
539
540 Armstrong, R.L., & Brodzik, M.J. (2002). Hemispheric-scale comparison and
541 evaluation of passive-microwave snow algorithms. *Annals of Glaciology, 34*, 38-44
542
543 Bair, E.H., Abreu Calfa, A., Rittger, K., & Dozier, J. (2018). Using machine learning
544 for real-time estimates of snow water equivalent in the watersheds of Afghanistan.
545 *Cryosphere, 12*
546
547 Boniface, K., Braun, J., McCreight, J., & Nievinski, F. (2015). Comparison of snow
548 data assimilation system with GPS reflectometry snow depth in the western United
549 States. *Hydrological Processes, 29*, 2425-2437
550
551 Brodzik, M.J. (2002). EASE-Grid: A versatile set of equal-area projections and grids.
552 *Discrete global grids*
553
554 Cao, Y., Yang, X., & Zhu, X. (2008). Retrieval snow depth by artificial neural network
555 methodology from integrated AMSR-E and in-situ data—A case study in
556 Qinghai-Tibet Plateau. *Chinese Geographical Science, 18*, 356-360
557
558 Chang, A., Foster, J., & Hall, D.K. (1987). Nimbus-7 SMMR derived global snow
559 cover parameters. *Annals of Glaciology, 9*, 39-44
560
561 Chang, A., & Tsang, L. (1992). A neural network approach to inversion of snow water
562 equivalent from passive microwave measurements. *Hydrology Research, 23*, 173-182
563 Che, T., Dai, L., Zheng, X., Li, X., & Zhao, K. (2016). Estimation of snow depth from
564 passive microwave brightness temperature data in forest regions of northeast China.
565 *Remote sensing of environment, 183*, 334-349
566
567 Che, T., Li, X., Jin, R., Armstrong, R., & Zhang, T. (2008). Snow depth derived from
568 passive microwave remote-sensing data in China. *Annals of Glaciology, 49*, 145-154

Chen, Y., Zhao, X., & Jia, X. (2015). Spectral–spatial classification of hyperspectral data based on deep belief network. *IEEE Journal of Selected Topics in Applied Earth Observations and Remote Sensing*, *8*, 2381-2392

Dai, L., Che, T., Wang, J., & Zhang, P. (2012). Snow depth and snow water equivalent estimation from AMSR-E data based on a priori snow characteristics in Xinjiang, China. *Remote sensing of environment*, *127*, 14-29

Davis, D.T., Chen, Z., Tsang, L., Hwang, J.-N., & Chang, A.T. (1993). Retrieval of snow parameters by iterative inversion of a neural network. *IEEE Transactions on Geoscience and Remote Sensing*, *31*, 842-852

Dietz, A.J., Kuenzer, C., Gessner, U., & Dech, S. (2012). Remote sensing of snow–a review of available methods. *International Journal of Remote Sensing*, *33*, 4094-4134

Evora, N.D., Tapsoba, D., & De Seve, D. (2008). Combining artificial neural network models, geostatistics, and passive microwave data for snow water equivalent retrieval and mapping. *IEEE Transactions on Geoscience and Remote Sensing*, *46*, 1925-1939

Foster, J., Chang, A., & Hall, D. (1997). Comparison of snow mass estimates from a prototype passive microwave snow algorithm, a revised algorithm and a snow depth climatology. *Remote sensing of environment*, *62*, 132-142

Gan, T.Y., Barry, R.G., Gizaw, M., Gobena, A., & Balaji, R. (2013). Changes in North American snowpacks for 1979–2007 detected from the snow water equivalent data of SMMR and SSM/I passive microwave and related climatic factors. *Journal of Geophysical Research: Atmospheres*, *118*, 7682-7697

Gan, T.Y., Kalinga, O., & Singh, P. (2009). Comparison of snow water equivalent retrieved from SSM/I passive microwave data using artificial neural network, projection pursuit and nonlinear regressions. *Remote sensing of environment*, *113*, 919-927

Grody, N.C., & Basist, A.N. (1996). Global identification of snowcover using SSM/I measurements. *IEEE Transactions on Geoscience and Remote Sensing*, *34*, 237-249

Gu, L., Ren, R., Zhao, K., & Li, X. (2014). Snow depth and snow cover retrieval from FengYun3B microwave radiation imagery based on a snow passive microwave unmixing method in Northeast China. *Journal of Applied Remote Sensing*, *8*, 084682

Ham, Y.-G. (2018). El Niño events will intensify under global warming. In: Nature Publishing Group

612 Hinton, G.E., Osindero, S., & Teh, Y.-W. (2006). A fast learning algorithm for deep
613 belief nets. *Neural computation, 18*, 1527-1554
614
615 Hinton, G.E., & Salakhutdinov, R.R. (2006). Reducing the dimensionality of data
616 with neural networks. *science, 313*, 504-507
617
618 Hu, X., Waller, L.A., Al-Hamdan, M.Z., Crosson, W.L., Estes Jr, M.G., Estes, S.M.,
619 Quattrochi, D.A., Sarnat, J.A., & Liu, Y. (2013). Estimating ground-level PM2. 5
620 concentrations in the southeastern US using geographically weighted regression.
621 *Environmental Research, 121*, 1-10
622
623 Huang, W., Song, G., Hong, H., & Xie, K. (2014). Deep architecture for traffic flow
624 prediction: deep belief networks with multitask learning. *IEEE Transactions on*
625 *Intelligent Transportation Systems, 15*, 2191-2201
626
627 Jia, Y., Jin, S., Savi, P., Gao, Y., Tang, J., Chen, Y., & Li, W. (2019). GNSS-R soil
628 moisture retrieval based on a XGboost machine learning aided method: Performance
629 and validation. *Remote Sensing, 11*, 1655
630
631 Kang, D.H., Shi, X., Gao, H., & Déry, S.J. (2014). On the changing contribution of
632 snow to the hydrology of the Fraser River Basin, Canada. *Journal of*
633 *Hydrometeorology, 15*, 1344-1365
634
635 Kelly, R.E., & Chang, A.T. (2003). Development of a passive microwave global snow
636 depth retrieval algorithm for Special Sensor Microwave Imager (SSM/I) and
637 Advanced Microwave Scanning Radiometer-EOS (AMSR-E) data. *Radio Science, 38*,
638 41-41-41-11
639
640 Langlois, A., Royer, A., Dupont, F., Roy, A., Goita, K., & Picard, G. (2011). Improved
641 corrections of forest effects on passive microwave satellite remote sensing of snow
642 over boreal and subarctic regions. *IEEE Transactions on Geoscience and Remote*
643 *Sensing, 49*, 3824-3837
644
645 Larson, K.M., Gutmann, E.D., Zavorotny, V.U., Braun, J.J., Williams, M.W., &
646 Nievinski, F.G. (2009). Can we measure snow depth with GPS receivers? *Geophysical*
647 *Research Letters, 36*
648
649 Larson, K.M., & Nievinski, F.G. (2013). GPS snow sensing: results from the
650 EarthScope Plate Boundary Observatory. *GPS solutions, 17*, 41-52
651
652 Li, L., Chen, H., & Guan, L. (2019). Retrieval of Snow Depth on Sea Ice in the Arctic
653 Using the FengYun-3B Microwave Radiation Imager. *Journal of Ocean University of*
654 *China, 18*, 580-588
655

Li, T., Shen, H., Yuan, Q., Zhang, X., & Zhang, L. (2017). Estimating ground-level PM2. 5 by fusing satellite and station observations: a geo-intelligent deep learning approach. *Geophysical Research Letters, 44*, 11,985-911,993

Liu, X., Jiang, L., Wang, G., Hao, S., & Chen, Z. (2018). Using a Linear Unmixing Method to Improve Passive Microwave Snow Depth Retrievals. *IEEE Journal of Selected Topics in Applied Earth Observations and Remote Sensing, 11*, 4414-4429

Liu, Y., Peters-Lidard, C.D., Kumar, S., Foster, J.L., Shaw, M., Tian, Y., & Fall, G.M. (2013). Assimilating satellite-based snow depth and snow cover products for improving snow predictions in Alaska. *Advances in water resources, 54*, 208-227

Mashtayeva, S., Dai, L., Che, T., Sagintayev, Z., Sadvakasova, S., Kussainova, M., Alimbayeva, D., & Akynbekkyzy, M. (2016). Spatial and temporal variability of snow depth derived from passive microwave remote sensing data in Kazakhstan. *Journal of Meteorological Research, 30*, 1033-1043

McCreight, J.L., Small, E.E., & Larson, K.M. (2014). Snow depth, density, and SWE estimates derived from GPS reflection data: Validation in the western US. *Water Resources Research, 50*, 6892-6909

Nievinski, F.G., & Larson, K.M. (2014). Inverse modeling of GPS multipath for snow depth estimation—Part II: Application and validation. *IEEE Transactions on Geoscience and Remote Sensing, 52*, 6564-6573

Rasmussen, R., Baker, B., Kochendorfer, J., Meyers, T., Landolt, S., Fischer, A.P., Black, J., Thériault, J.M., Kucera, P., & Gochis, D. (2012). How well are we measuring snow: The NOAA/FAA/NCAR winter precipitation test bed. *Bulletin of the American Meteorological Society, 93*, 811-829

Rodriguez, J.D., Perez, A., & Lozano, J.A. (2010). Sensitivity analysis of k-fold cross validation in prediction error estimation. *IEEE transactions on pattern analysis machine intelligence, 32*, 569-575

Rosenfeld, S., & Grody, N. (2000). Anomalous microwave spectra of snow cover observed from Special Sensor Microwave/Imager measurements. *Journal of Geophysical Research: Atmospheres, 105*, 14913-14925

Rostosky, P., Spreen, G., Farrell, S.L., Frost, T., Heygster, G., & Melsheimer, C. (2018). Snow depth retrieval on Arctic sea ice from passive microwave radiometers—Improvements and extensions to multiyear ice using lower frequencies. *Journal of Geophysical Research: Oceans, 123*, 7120-7138

Rumelhart, D.E., Hinton, G.E., & Williams, R.J. (1988). Learning representations by back-propagating errors. *Cognitive modeling, 5*, 1

Santi, E., Pettinato, S., Paloscia, S., Pampaloni, P., Fontanelli, G., Crepaz, A., & Valt, M. (2014). Monitoring of Alpine snow using satellite radiometers and artificial neural networks. *Remote sensing of environment, 144*, 179-186

Santi, E., Pettinato, S., Paloscia, S., Pampaloni, P., Macelloni, G., & Brogioni, M. (2012). An algorithm for generating soil moisture and snow depth maps from microwave spaceborne radiometers: HydroAlgo. *Hydrology and Earth System Sciences, 16(10), 3659-3676*

Shi, J., Xiong, C., & Jiang, L. (2016). Review of snow water equivalent microwave remote sensing. *Science China Earth Sciences, 59*, 731-745

Shi, X., Marsh, P., & Yang, D. (2015). Warming spring air temperatures, but delayed spring streamflow in an Arctic headwater basin. *Environmental Research Letters, 10*, 064003

Singh, P.R., & Gan, T.Y. (2000). Retrieval of snow water equivalent using passive microwave brightness temperature data. *Remote sensing of environment, 74*, 275-286

Song, X., Zhang, G., Liu, F., Li, D., Zhao, Y., & Yang, J. (2016). Modeling spatio-temporal distribution of soil moisture by deep learning-based cellular automata model. *Journal of Arid Land, 8*, 734-748

Specht, D.F. (1991). A general regression neural network. *IEEE transactions on neural networks, 2*, 568-576

Tabari, H., Marofi, S., Abyaneh, H.Z., & Sharifi, M. (2010). Comparison of artificial neural network and combined models in estimating spatial distribution of snow depth and snow water equivalent in Samsami basin of Iran. *Neural Computing and Applications, 19*, 625-635

Tabibi, S., Geremia-Nievinski, F., & van Dam, T. (2017). Statistical comparison and combination of GPS, GLONASS, and multi-GNSS multipath reflectometry applied to snow depth retrieval. *IEEE Transactions on Geoscience and Remote Sensing, 55*, 3773-3785

Tedesco, M., Derksen, C., Deems, J.S., & Foster, J.L. (2015). Remote sensing of snow depth and snow water equivalent. *Remote sensing of the cryosphere*, 73-98

Tedesco, M., Pulliainen, J., Takala, M., Hallikainen, M., & Pampaloni, P. (2004). Artificial neural network-based techniques for the retrieval of SWE and snow depth from SSM/I data. *Remote sensing of environment, 90*, 76-85

743 Tsutsui, H., & Maeda, T. (2017). Possibility of estimating seasonal snow depth based
744 solely on passive microwave remote sensing on the greenland ice sheet in Spring.
745 *Remote Sensing*, *9*, 523
746
747 Ulaby, F.T., & Stiles, W.H. (1980). The active and passive microwave response to
748 snow parameters: 2. Water equivalent of dry snow. *Journal of Geophysical Research:*
749 *Oceans*, *85*, 1045-1049
750
751 Vey, S., Güntner, A., Wickert, J., Blume, T., Thoss, H., & Ramatschi, M. (2016).
752 Monitoring snow depth by GNSS Reflectometry in built-up areas: A case study for
753 Wettzell, Germany. *IEEE Journal of Selected Topics in Applied Earth Observations*
754 *and Remote Sensing*, *9*, 4809-4816
755
756 Wang, J., Song, C., Reager, J.T., Yao, F., Famiglietti, J.S., Sheng, Y., MacDonald,
757 G.M., Brun, F., Schmied, H.M., & Marston, R.A. (2018). Recent global decline in
758 endorheic basin water storages. *Nature geoscience*, *11*, 926-932
759
760 Wang, W., Huang, X., Deng, J., Xie, H., & Liang, T. (2015). Spatio-temporal change
761 of snow cover and its response to climate over the Tibetan Plateau based on an
762 improved daily cloud-free snow cover product. *Remote Sensing*, *7*, 169-194
763
764 Wu, X., Che, T., Li, X., Wang, N., & Yang, X. (2018). Slower snowmelt in spring
765 along with climate warming across the Northern Hemisphere. *Geophysical Research*
766 *Letters*, *45*, 12,331-312,339
767
768 Xiao, X., Zhang, T., Zhong, X., Shao, W., & Li, X. (2018). Support vector regression
769 snow-depth retrieval algorithm using passive microwave remote sensing data. *Remote*
770 *sensing of environment*, *210*, 48-64
771
772 Xu, H., Yuan, Q., Li, T., Shen, H., Zhang, L., & Jiang, H. (2018). Quality
773 Improvement of Satellite Soil Moisture Products by Fusing with In-Situ
774 Measurements and GNSS-R Estimates in the Western Continental US. *Remote*
775 *Sensing*, *10*, 1351
776
777 Zhang, S., Wang, X., & Zhang, Q. (2017). Avoiding errors attributable to topography
778 in GPS-IR snow depth retrievals. *Advances in Space Research*, *59*, 1663-1669
779